3D MAPPING OF PORE AND ORGANIC MATTER DISTRIBUTIONS IN UNCONVENTIONAL RESERVOIRS UTILIZING A DIGITAL ROCKS APPROACH

Andrew Fogden, Jill Middleton, Thomas McKay, Shane Latham, Rohini Marathe, Michael Turner, Adrian Sheppard, Australian National University, Canberra
James J. Howard, F. David Lane, ConocoPhillips, Bartlesville, OK

This paper was prepared for presentation at the International Symposium of the Society of Core Analysts held in Avignon, France, 8-11 September, 2014

ABSTRACT

The fine-grained nature of many unconventional reservoir rocks poses severe challenges for routine and special core analyses. A digital rocks approach to generate pore- and grain-network models for calculation of flow and mechanical properties is an appealing alternative, but presents its own set of imaging challenges. In this study, mini-plugs from four unconventional carbonate-rich samples were imaged by micro-CT in a sequence of states designed to selectively enhance X-ray attenuation contrast and resolution. Pressure saturation by diiodomethane enormously boosted the attenuation of pores such that even sparse micro/nano-porosity became appreciably brightened. Exposure to iodine stained the organic matter to highlight its distribution. Registration and differencing of the mini-plug tomograms acquired in these states then provided separate 3D maps of porosity and organic matter for image analysis. Segmentation yielded overall volume fractions in good agreement (within 20% relative error) with porosity and TOC measured on core plugs. Scatter histograms gave statistical measures to type the unconventional sample according to its relative populations of features locally rich or lean in porosity and/or organic matter. Higher resolution SEM images of an ion-milled section through the mini-plug and its registration into the tomograms provided a means to associate pore morphologies and sizes to these features towards construction of a 3D map of preferred flow pathways.

INTRODUCTION

The dramatic shift in the production of hydrocarbons from conventional reservoirs to more recent efforts focused on unconventional reservoirs poses many challenges for core analysis and its role in providing key parameters for reservoir simulation and modeling [1]. Definitions of unconventional reservoirs vary, but they converge on rocks with sufficiently low porosity and permeability to require new production strategies. This constraint carries over to the realm of core analysis where samples with permeability below a micro-Darcy are not amenable to standard techniques [2]. The limitations on core analysis of unconventionals include cleaning, estimation of pore volume and fluid saturations, and measurement of transport properties. Inability to remove all fluids from pores during cleaning creates problems with identifying a starting point for any traditional SCAL program. In essence, an entirely new approach for analysis of unconventional reservoir petrophysical properties needs to be developed.

The digital rocks approach determines the values of various petrophysical properties by solution of basic flow equations and other models on a numerical network representing the pore- or grain-space [3]. Further, the smaller samples used for imaging are easier to clean and establish well-characterized initial conditions. X-ray micro-tomography (micro-CT) is the standard imaging method of digital core analysis of conventional reservoir rocks [4]. Owing to the fine-grain nature of unconventionals, ultra-high resolution imaging of 2D section surfaces by FE-SEM and small 3D regions by FIB-SEM is necessary to distinguish nanoscale pores and organic matter (OM) details [5-6]. Micro-CT could provide the structural link between these microscopic volumes and plug scale. However, this requires a means to overcome the lack of sensitivity of X-ray attenuation to distinguish pore from OM. Previous studies have demonstrated the utility of scanning conventional rock samples in their dry state and again after saturation with an attenuating liquid, such that spatial alignment and subtraction of the two tomograms highlights all accessible pores [4]. A primary goal of the current study is to adapt this approach to quantify the volume and distribution of pores and OM in unconventional subsamples.

EXPERIMENTAL

Core Plugs

Samples were selected from a sequence of fine-grain carbonate rock, interbedded with layers of fossiliferous packstone chalk and organic-rich marls composed predominately of calcite with quartz, clay minerals, pyrite and OM distributed through the matrix. The original sediment was deposited as a carbonate mud in shallow marine environments. The compacted organic-rich marls and chalk contain considerable inter-particle porosity and variable intra-particle porosity in microfossils. Diagenetic processes and geochemical alteration transformed many microfossils into solid carbonate particles, while others remained porous and nucleated authigenic clays. The pore volume is associated with the fine-grain matrix, microfossil fragments and other detritus, together with the OM, generally identified as kerogen, and between authigenic clay particles.

From four depths, a pair of core plugs (25.6 mm diameter) was cut perpendicular (*i.e.* vertical, V) or parallel (horizontal, H) to bedding. Table 1 lists the composition of the samples, denoted S1-S4. Porosity (from NMR measurement of liquid content followed by Helium porosimetry), TOC (LECO carbon analyzer) and kerogen content (petrographic analysis) increase from S1 through to S4, as is often observed for gas shales [5-6]. The organic lean S1 and S2 represent the extremes of carbonate, clay and pyrite contents, while the mineral compositions of the organic rich S3 and S4 are more similar.

Table 1. Measured composition of the four samples from vertically cored plugs.

Sample	Porosity (%)	TOC (wt %)	Kerogen (vol %)	Carbonate (wt %)	Clay (wt %)	Quartz Plagio-clase (wt %)	Pyrite (wt %)
S1V	4.3	1.78	4.0	76.3	9.6	13.3	0.8
S2V	5.2	2.56	6.0	37.3	37.0	21.1	4.2
S3V	5.8	4.93	11.8	57.5	17.2	22.6	1.6
S4V	7.6	5.55	12.1	53.8	25.8	17.9	2.2

Mini-plugs and Preparation for Micro-CT

Tomographic data of the S1-S4 vertically cored plugs and their subsamples were acquired, processed and analyzed at the ANU micro-CT facility using MANGO software [4]. Most scans were performed on a Heliscan micro-CT with a double-helical trajectory [7], rotating and vertically translating the sample through a filtered polychromatic X-ray beam to capture 2520 projections per pitch on a flat panel detector (2048x1536 pixel^2) at a source distance of 330 mm. The tomogram was 1800 voxel wide and spanned the full height of the sectioned plugs and shorter mini-plugs or the middle of taller mini-plugs. The core plugs were scanned at 110 kV and 130 μA at 15.6 μm/voxel resolution. A location in the tomogram was selected for vertical subsampling (parallel to the plug axis, perpendicular to bedding). A 3 mm diameter mini-plug of 3-7 mm height was cored there using a manually-fed drill press with diamond bit and air as lubricant.

A sequence of four high-resolution (2.0 μm/voxel) tomograms of each mini-plug, usually in an aluminum holder, was acquired at 80 kV and 110 μA. After the first scan of its initial state, the mini-plug was mildly cleaned in toluene and methanol to remove residual liquid hydrocarbons and brine. Its pore space was then highlighted by invasion of the highly X-ray attenuating liquid diiodomethane (CH_2I_2) via evacuation for 12 h, vacuum infiltration for 24 h, then cyclical isostatic pressurization to 20 MPa in CH_2I_2 over 36 h. This second state was scanned in a corrosion-resistant titanium holder filled with CH_2I_2. The third scan of the mini-plug was in its post-dry state after removal of CH_2I_2 by immersion in toluene for 14 days. It was then evacuated for 1 h and infiltrated with 2.5 wt% solution of iodine (I_2) in toluene for 6 h, followed by 14 days of ambient immersion. The mini-plug was then vacuum dried for 14 days to evaporate toluene and free I_2 to leave only the I_2 bound to, and thus highlighting, the OM in the scan of this fourth state.

RESULTS AND DISCUSSION

CT and Petrophysical Properties of Core Plugs

A vertical tomogram slice of the vertically cored plug sections is shown in Figure 1. Very few features are visible at this resolution, aside from faint horizontal laminations around 5 mm thick. Darker horizontal bands of lower X-ray attenuation are richer (*i.e.* higher) in porosity and/or OM, and the bright specks of high density mineral correspond to pyrite (Table 1). Fracture-like features (most prevalent in S4V) tend not to traverse the entire diameter of the plugs and terminate at their edge. They are interpreted as coring-induced partings, and are presumably responsible for limiting the height of the intact mini-plugs.

Petrophysical measurements on the companion horizontal and vertical core plugs at 1810 psi confining pressure are given in Table 2. Resistivity, permeability and velocity display varying degrees of sample anisotropy. Resistivity (inversely the electrical conductivity) of the vertical plugs is greater than their horizontal counterparts, as expected, and indicates that S4 and S2 have most anisotropy while S3 is most uniform. Three of the pairs show the expected trend of horizontal permeability greater than vertical, including S3 since S3V fell below the 5 nD detection limit of the pulse decay apparatus. Several plugs have permeability values below this limit, which illustrates some of the challenges

in measuring such tight rocks. One such sample, S1H, falls outside the expected response with a lower permeability than S1V, while S4 and S2 again display strong anisotropy. In general, neither resistivity nor permeability follows a trend with porosity in Table 1.

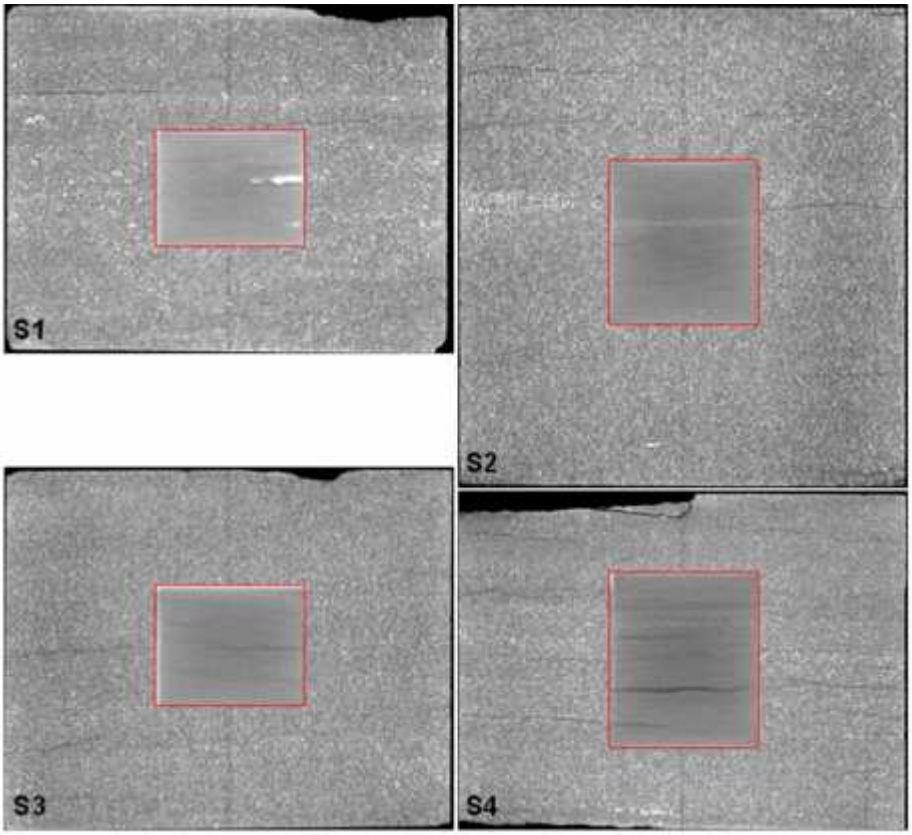

Figure 1. Central vertical slice of the four vertically cored plugs, with fields of view of width 25.4 mm and heights (in mm) S1V: 19.8, S2V: 27.5, S3V: 20.4, S4V: 19.1. Inset: tomogram slice acquired at higher kV.

Table 2. Permeability, resistivity and ultrasonic compressional and shear velocity of the horizontally and vertically cored plugs, measured at a confining pressure of 1810 psi.

Sample	Permeability (nD)	Rt (Ohm-m)	Vp (km/sec)	Vs (km/sec)
S1H	2.8	56.7	5.24	2.96
S1V	11.7	101.3	4.54	2.70
S2H	101.6	82.6	4.61	2.59
S2V	10.9	737.9	4.03	2.31
S3H	12.0	334.2	4.77	2.81
S3V	-	402.9	3.98	2.28
S4H	62.0	96.0	4.67	2.74
S4V	2.2	857.4	3.80	2.26

The horizontally cored plugs have faster compressional and shear velocities than their vertical counterparts. Both velocities for vertical plugs tend to decrease with porosity in Table 1, as expected. Figure 2 complements the Table 2 results with compressional

velocity measured at two lower confining pressures of 400 and 1000 psi. Confining pressure has little effect on velocity for the horizontal plugs, as their partings run parallel to their long axis and to the direction of sound propagation. A 400 psi confining pressure suffices to compress these partings to have minimal impact on measured velocities. The velocities of vertically cored plugs increase as much as 20% as confining pressure increases from 400 to 1810 psi. Their partings are perpendicular to the sound propagation and are more affected by the radially-directed confining pressure. The strong and variable influence of partings on plug-scale petrophysical measurements makes it difficult to isolate the true contribution of anisotropy due to bedding on transport and elastic properties. The higher-resolution, contrast-enhanced tomography of the mini-plugs, albeit limited in height by these partings, gives insight into the underlying pore, OM and grain networks from millimeters down to microns, as outlined in the remainder of the paper.

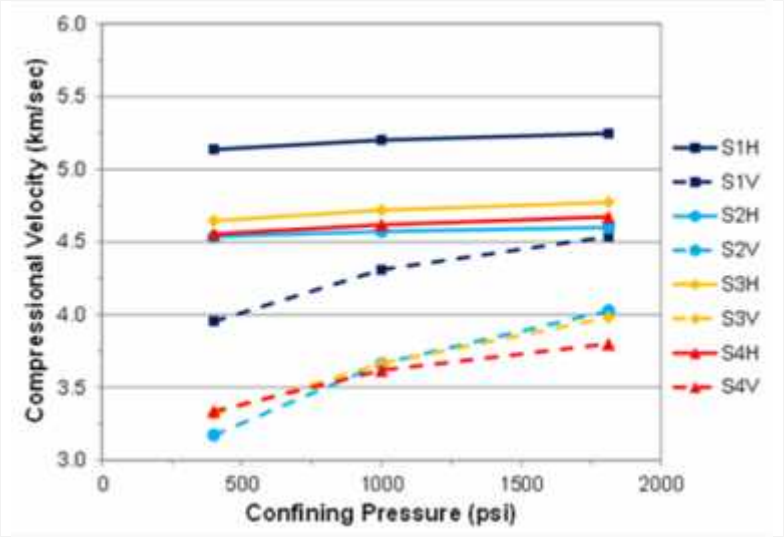

Figure 2. Variation in ultrasonic compressional velocity as function of confining pressure for horizontally and vertically cored plugs of samples S1-S4.

Distribution of Porosity and Organic Matter in Mini-Plugs

The left column of Figure 3 shows a vertical tomogram slice of the four mini-plugs cored perpendicular to bedding. The outermost 100 voxels were masked from the edge where residual beam hardening artifacts become significant. The higher resolution serves to resolve calcite particles (light gray) and individual pyrite clusters (bright). In S1-S3 the former are primarily planispiral foraminifera, preserved as compacted tests infilled with calcite spar. These ball-shaped particles are sometimes merged, and other elongated particles and more irregular fragments are also common. The particles in S3 are finer than in S1 and S2, while those of S4 are so small as to be largely unresolvable. Pyrite is a replacement mineral in the foraminifera, especially around their rims in S3, and also dots the matrix. Horizontal lamination is faintly visible in S1-S3, as grain-rich or -poor bands around one-third down the S1 and S3 slice (where the yellow profile weakly peaks or dips, respectively), and by the tendency for elongated grains in S2 and S3 to lie flat. More pronounced lamination in S4 is seen by the short- and long-scale variations in its profile.

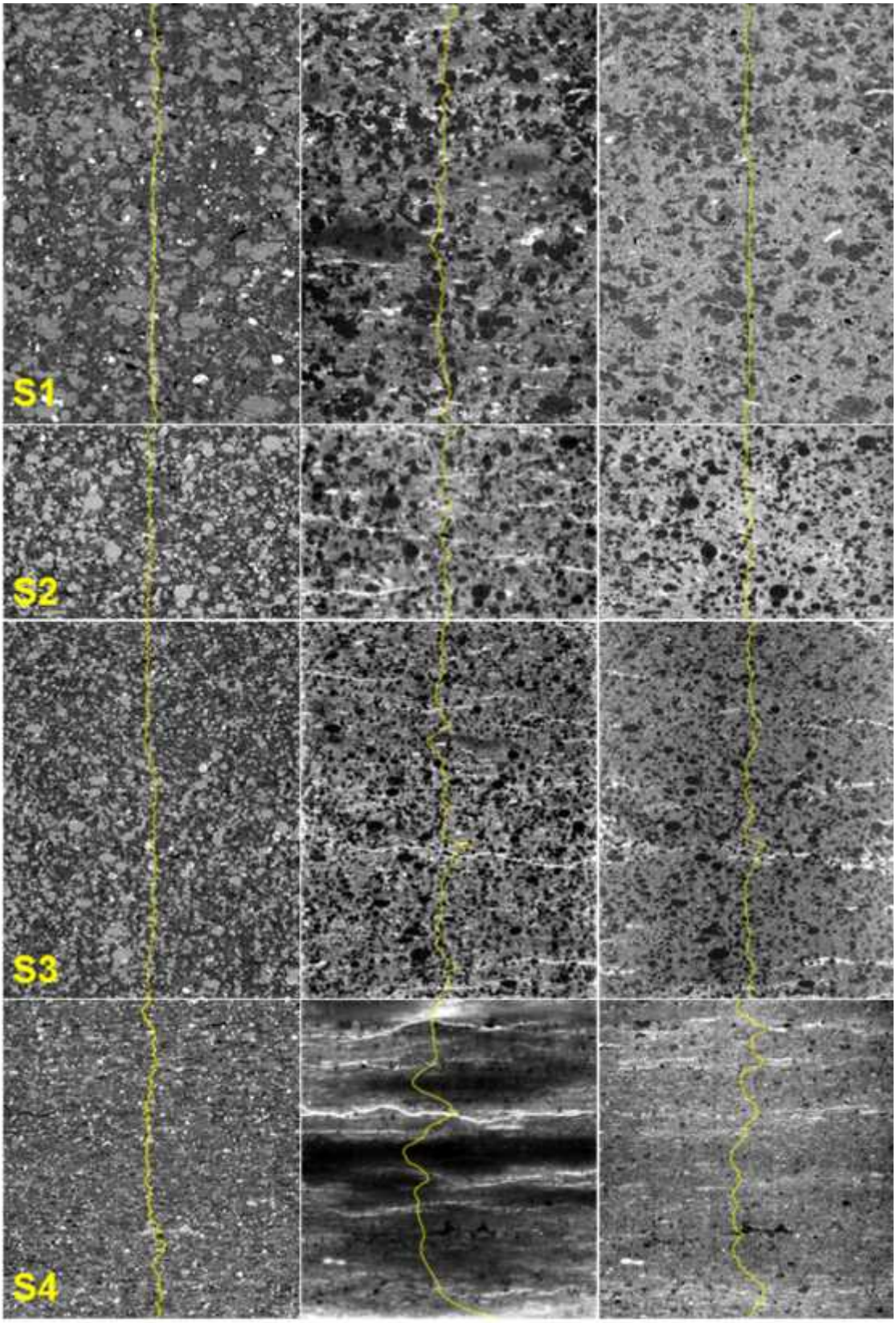
S1
S2
S3
S4

Figure 3. Central vertical masked slice of the four vertically cored mini-plugs, in the initial state (left) and after the differences: CH_2I_2-infiltrated minus post-dry (middle) and I_2-stained minus initial (right), with fields of view (in mm) S1: 2.4x3.5, S2: 2.9x1.9, S3: 2.8x3.6, S4: 2.4x2.6. Yellow curves are (horizontally-averaged) longitudinal profiles of tomogram attenuation in arbitrary units.

Dark features are apparent in the left column of Figure 3 as occasional fine partings and as chamber, slot or strand forms. Even at this higher resolution, these features cannot be reliably distinguished as pore or OM or both, due to the similarly low X-ray attenuation of air and kerogen. Further, much smaller pores and OM domains are presumably also intermingled in the featureless matrix of similarly fine mineral particles. The grayscale of such matrix voxels reflects the attenuation sum from all unresolved components present there, and the proportions of each cannot be determined without additional information.

The contrast strategy in the Experimental section was thus employed. The mini-plug was imaged in three sequential states (CH_2I_2 infiltrated, post-dry and I_2 stained), which were registered [4] to overlay the initial tomogram. CH_2I_2 is a reference apolar liquid in the contact angle literature and wets most minerals in air [8]. Its infiltration greatly boosts pore attenuation; even voxels with only sparse micro/nano-porosity are appreciably brightened. A side effect is slight staining of OM, probably by its binding of free I_2 from CH_2I_2 radiolysis during scanning. After CH_2I_2 extraction, the post-dry state restores the low pore attenuation, while OM retains most of this weak staining. Subtraction of the post-dry tomogram from its CH_2I_2-infiltrated (registered) counterpart thus cancels the attenuation of the unchanged minerals and OM to yield a 3D map of porosity. In the final imaged state, OM is completely stained by bound I_2, while all other constituents remain unchanged, so subtraction of the initial state from this tomogram produces a map of OM.

The middle and right columns of Figure 3 show the same slice (as for the initial state at left) of these two difference tomograms highlighting porosity and OM, respectively. The left and middle columns of Figure 4 give zoom-ins of a subset of the corresponding slice, identifying typical feature types with letters (see Table 3, sometimes followed by number subtypes) based on the local intensity of the CH_2I_2-infiltrated minus post-dry tomogram (with brighter representing higher porosity) and the I_2-stained minus initial tomogram (with brighter indicating more OM). The latter difference is noisier since I_2 uptake by OM gives a significantly smaller boost to attenuation than bulk CH_2I_2 filling pores.

Features **A** are darkest in both differences and are solid mineral, while **B** denotes the matrix, where features are indistinguishable but pore or OM gives a lighter grayscale in the difference than for **A**. Nearly every matrix voxel has at least some porosity and OM. CH_2I_2 reveals variations in matrix micro/nano-porosity, despite the lack of anomalous structure there in the initial-state image. The stronger laminations of the S4 mini-plug (and core plug in Figure 1) are fully revealed in its contrasted tomograms. While **A** and **B** occupy the majority of tomogram volume, other features are of interest as their form is at least partly resolvable. Features **C** take up CH_2I_2 but not I_2, as do partings **D,** while **G** take up I_2 but not CH_2I_2 and **F** take up both. Some initially dark chambers **U** remain unhighlighted, despite CH_2I_2 and I_2 accessing features in their immediate neighborhood.

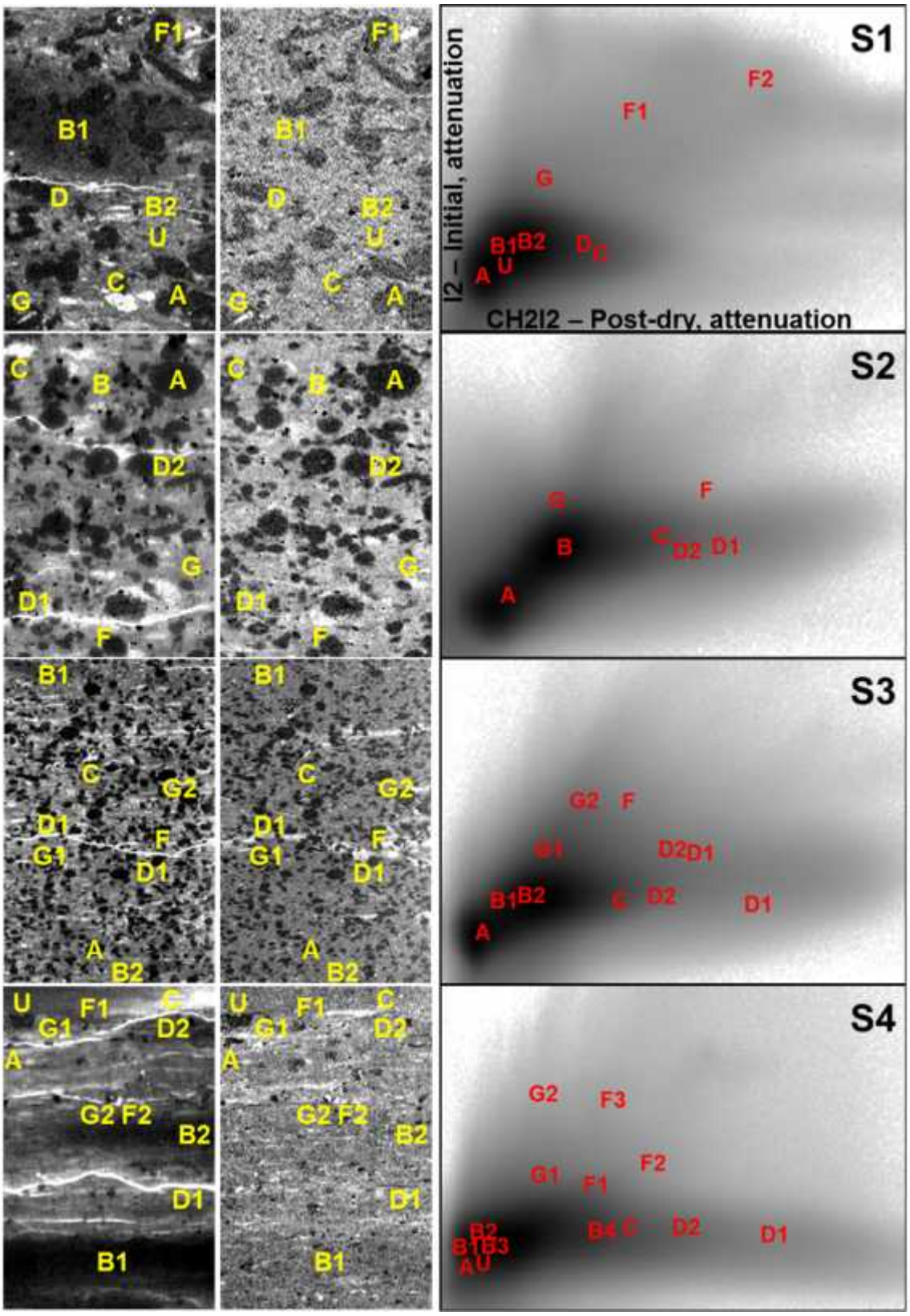
F1
B1
D
B2
U
C
A
G
C
B
A
D2
G
D1
F
B1
C
G2
D1
F
G1
D1
A
B2
U
F1
C
G1
D2
A
G2 F2
B2
D1
B1
S1
S2
S3
S4
I2 – Initial, attenuation
CH2I2 – Post-dry, attenuation
F2
F1
G
B1
B2
D
C
A
U
F
E
B
C
D2
D1
A
G2
F
E1
D2
D1
B1
B2
C
D2
D1
A
F3
F2
G1
F1
B2
B4
C
D2
D1
B3
A
U

Figure 4. Central vertical slice subset of the registered tomogram differences: CH_2I_2-infiltrated minus post-dry (left) and I_2-stained minus initial (middle) of the four mini-plugs, with fields of view (in mm) S1: 0.71x1.09, S2: 0.77x1.17, S3: 1.37x2.10, S4: 0.94x1.44. At right is the histogram of frequency of their voxel attenuation differences over the entire masked tomogram volume.

Table 3. Feature types identified in samples S1-S4 (as labeled in Figure 4).

Type	Characteristics	Occurrence and Examples
A	Solid mineral grains Non-porous and OM-free	Resolvable calcite particles in S1-S3 (with occasional tiny pore), but only few in S4. Pyrite (but differences least reliable due to high attenuation and local beam hardening artifacts).
B	Matrix of sub-resolution features containing some porosity and OM	S2 matrix most uniform (but limited height imaged). S1 and S3 matrix regions vary from lower micro/nano-porosity (**B1**, center left of S1 in Figure 3) to higher (**B2**). S4 bands of vastly differing micro/nano-porosity, from very low (**B1**) to high (**B4**).
C	Porosity rich but OM lean	In S1-S3 as separate irregular granular shapes or anisotropic slots in more laminated regions (especially S3). Are micro/nano-porous rather than macropores as seldom coincide with resolvable dark features in initial state. Relatively rare in S4.
D	Partings and hair-line partings (**D2**)	Possibly coring-induced. Parting surrounds in S1-S2 are OM lean. Parting surrounds in S3-S4 are often OM rich.
F	OM-hosted porosity	**F** and **G** in S1-S2 coincide with dark features in initial state. **F** and **G** in S3-S4 often lie near partings. In S4 (Figure 4), **F1** and **G1** are slot-formed, **F2** and **G2** are chambers.
G	OM rich but porosity lean	Effectively solid OM. See above
U	OM and/or pore macro-chambers unhighlighted	Inaccessible or fail to bind I_2. Seen in S1 (examples in Figure 3 slice) and S4.

These observations can be quantified by a 2D scatter histogram of voxel frequency versus their (arbitrarily scaled) attenuation in the CH_2I_2 and I_2 difference tomograms, shown in the right column of Figure 4. The dark cloud covers most voxels. Its bottom left lobe for S1-S3 represents solid mineral **A** while its remainder is from the featureless matrix **B**, with its spread indicative of variations in sub-resolution porosity and OM. Two arms emanate from it; the roughly horizontal one represents progressively more porosity-dominated features (**C** and **D**) while the roughly vertical arm represents increasingly OM-dominated features **G**. Features **F** rich in both porosity and OM lie between the two arms. The arms tend to strengthen and converge from S1 through to S4, signifying increasing porosity and OM and their increasing co-location. This transition is not due to a rising population of distinct OM-hosted pore features **F**, but rather by partings **D** incorporating more OM. For S4, the solid mineral **A** is largely absent in Figure 4 and the dark cloud is dilated by the large variations in matrix porosity. Its OM-rich arm has largely collapsed onto the pore-rich horizontal arm and raised its baseline organic content.

Segmentation was performed to convert attenuation of the CH_2I_2 difference tomogram into porosity. Brightest and darkest features bounded by steep gradients were used to set

the thresholds of 100% and 0% porous voxels, from which a converging active contours algorithm identified the macro-pore and macro-solid phases [4]. Microporosity was taken as linear in grayscale between these two thresholds. The same procedure applied to the I_2 difference quantified macro- and micro-OM. Further, pyrite was segmented as the bright phase in the initial tomogram. Table 4 lists the overall values for the mini-plug masked tomogram. Total porosity and OM (kerogen) volume fraction are in good agreement with the core plug measurements in Table 1. Substantial downscaling can apparently preserve a reasonable representation of composition, but less so for the more laminated S3 and S4. The segmentations contain fairly large uncertainties due to lack of macro-pores. Increase of the macro-pore threshold by 1% of the sample's grayscale range would increase total porosity by ~0.07 p.u. The analysis also assumes that all kerogen in a mini-plug has equal chemical binding capacity for I_2 per volume, and omits the small contribution from pores or OM in **U** features. Comparing Tables 1 and 4, the segmented pyrite content of the S1-S4 mini-plugs follows a similar hierarchy as that of the core plug material used for XRD.

Table 4. Volume fractions of pyrite, and accessible macro-, micro- and total porosity and organic content of mini-plugs S1-S4 estimated from tomogram segmentation.

	Pyrite (vol%)	Porosity (vol%)			Organic (vol%)		
Sample	Total	Macro	Micro	Total	Macro	Micro	Total
S1	1.46	0.00	4.51	4.51	0.00	4.01	4.01
S2	2.67	0.00	5.22	5.22	0.01	5.95	5.96
S3	2.28	0.00	6.18	6.18	0.01	10.03	10.04
S4	2.25	0.00	9.03	9.03	0.02	11.74	11.76

The four mini-plugs were sectioned crosswise and one face was ion milled and carbon coated for acquisition of a grid of FE-SEM images. Figure 5 (upper panel) shows the stitched image of the S1 face, at the center of which a finer grid was acquired at 10 times higher resolution (red rectangle). The 2D face map was registered into the mini-plug tomogram sequence. Figure 5 (lower panels) shows the same subarea (corresponding to the upper yellow rectangle) of the higher resolution FE-SEM map, the initial tomogram and the CH_2I_2- and I_2-contrasted difference tomograms. The bright, light gray, dark and intermediate-grayscale regions of the initial tomogram overlay regions in FE-SEM of pyrite, calcite, OM and mixed micro/nano-mineral/pore/OM, respectively (although beam hardening artifacts can be seen near the central pyrite crystal). Further, CH_2I_2 and I_2 tend to preferentially brighten locations in FE-SEM rich in porosity and OM, respectively. **C**, **F** and **G** features in these tomogram differences generally correspond to mineral-hosted micro/nano-porosity, OM-hosted pores and solid OM, respectively. This validates the X-ray contrast strategy of this study. In spite of its almost two orders of magnitude lower resolution than FE-SEM, the CH_2I_2 difference tomogram pinpoints local variations in porosity with high fidelity. The I_2 difference is somewhat less impressive, due to the weaker contrast of OM staining. In other regions of this S1 face, some solid OM domains were unhighlighted by I_2, suggesting that lack of I_2 binding rather than CH_2I_2 saturation was responsible for the lack of highlighting of some dark regions in the initial tomogram of S1 and S4. Further work should address the specificity of I_2 binding to kerogen types.

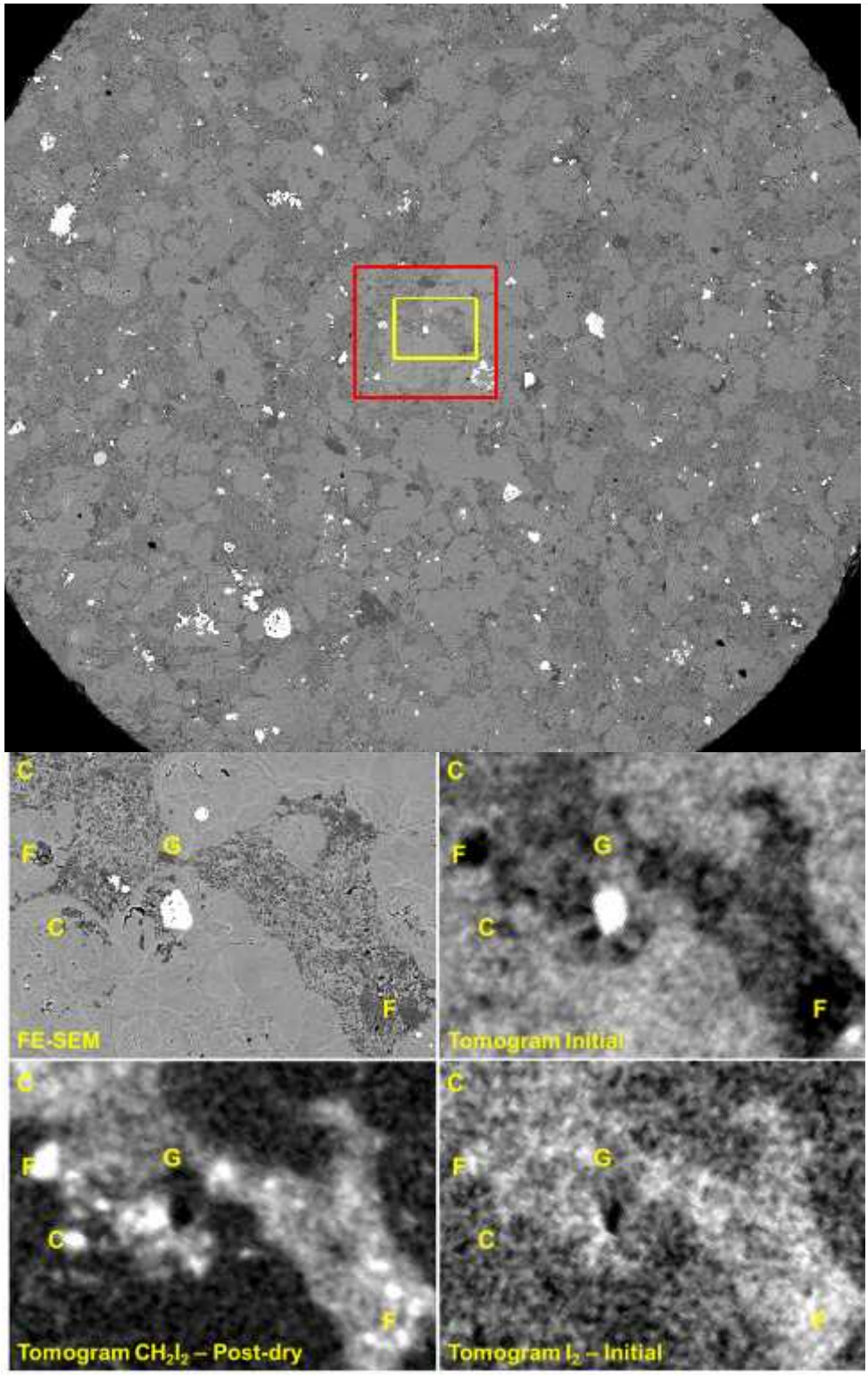

Figure 5. Upper: FE-SEM stitched map (2.61 mm x 2.28 mm, at 0.34 µm/pixel resolution) of ion-milled section of S1 mini-plug parallel to bedding. Lower: subarea (248 µm x 179 µm, at 0.034 µm/pixel) of FE-SEM map and of the registered tomograms in the initial state and the two contrasted differences.

CONCLUSION

While the imaged volumes and spatial resolutions of micro-CT are well suited to non-destructive 3D mapping of unconventional subsamples on the meso-scales (within laminations) bridging core plugs and micron-sized FIB-SEM fields of view, the weak attenuation of pores and OM has posed a major limitation. Use of the X-ray contrast strategies (diiodomethane for pores and iodine for organic) and tomogram registration in this study revealed the types of pore-rich and/or OM-rich features present on 10-1000 μm scales and also facilitated extraction of pore and organic volumes per voxel from sub-resolution scales. Overall volume fractions lay within 20% of plug measurements. Higher resolution SEM and its registration into the tomograms can then serve to identify the micro/nano-pore sizes, shapes and connectivities characteristic of each micro-CT feature type. This will aid in determining the preferred transport pathways through unconventional plugs and the grain network (and its heterogeneities) dictating their mechanical properties.

ACKNOWLEDGEMENTS

ANU thanks the member companies of the DigiCore Consortium for financial support.

REFERENCES

1. Rosen, R., W. Mickelson, M. Sharf-Aldin, *et al.* 2014. Impact of Experimental Studies on Unconventional Reservoir Mechanisms, *Proceedings of SPE Unconventional Resources Conference*, SPE-168965.
2. Sinha, S., E. Braun, M. Determan, *et al.* 2013. Steady-State Permeability Measurements on Intact Shale Samples at Reservoir Conditions – Effect of Stress, Temperature, Pressure and Type of Gas, *Proceedings of SPE Middle East Oil and Gas Show and Conference*, SPE-164263.
3. Dvorkin, J., N. Derzhi, E. Diaz, *et al.* 2011. Relevance of computational rock physics. *Geophysics* **76**: E141-E153.
4. Sheppard, A., S. Latham, J. Middleton, *et al.* 2014. Techniques in helical scanning, dynamic imaging and image segmentation for improved quantitative analysis with X-ray micro-CT. *Nuclear Instruments and Methods in Physics Research B* **324**: 49-56.
5. Milliken, K.L., M. Rudnicki, D.N. Awwiller, *et al.* 2013. Organic matter-hosted pore system, Marcellus Formation (Devonian), Pennsylvania. *AAPG Bulletin* **97**: 177-200.
6. Sondergeld, C., K. Newsham, J. Comisky, *et al.* 2010. Petrophysical Considerations in Evaluating and Producing Shale Gas Resources, *Proceedings of SPE Unconventional Gas Conference*, SPE 131768.
7. Varslot, T., A. Kingston, G. Myers, *et al.* 2011. High-resolution helical cone-beam micro-CT with theoretically-exact reconstruction from experimental data. *Medical Physic*s 38: 5459.
8. Shang, J., M. Flury, J.B. Harsh, *et al.* 2008. Comparison of different methods to measure contact angles of soil colloids. *J. Colloid Interface Sci.* 328: 299-307.